Fabrication of High-Aspect Ratio Nanogratings for Phase-Based X-Ray Imaging

Martyna Michalska, Alessandro Rossi, Gašper Kokot, Callum M. Macdonald, Silvia Cipiccia, Peter R.T. Munro, Alessandro Olivo,* and Ioannis Papakonstantinou*

Diffractive optical elements such as periodic gratings are fundamental devices in X-ray imaging – a technique that medical, material science, and security scans rely upon. Fabrication of such structures with high aspect ratios at the nanoscale creates opportunities to further advance such applications, especially in terms of relaxing X-ray source coherence requirements. This is because typical grating-based X-ray phase imaging techniques (e.g., Talbot self-imaging) require a coherence length of at least one grating period and ideally longer. In this paper, the fabrication challenges in achieving high-aspect ratio nanogratings filled with gold are addressed by a combination of laser interference and nanoimprint lithography, physical vapor deposition, metal assisted chemical etching (MACE), and electroplating. This relatively simple and cost-efficient approach is unlocked by an innovative post-MACE drying step with hexamethyldisilazane, which effectively minimizes the stiction of the nanostructures. The theoretical limits of the approach are discussed and, experimentally, X-ray nanogratings with aspect ratios >40 are demonstrated. Finally, their excellent diffractive abilities are shown when exposed to a hard (12.2 keV) monochromatic X-ray beam at a synchrotron facility, and thus potential applicability in phase-based X-ray imaging.

1. Introduction

The ability to fabricate high-aspect ratio silicon nano-structures is fundamental in many applications spanning

sensors,[1] batteries,[2] solar cells,[3] super-hydrophobic,[4,5] and mechano-bactericidal materials[6] as well as X-ray imaging.[7,8] Diffractive optics such as periodic nanogratings are key to separating wavelengths and generating iridescent colors, useful further in information storage,[9] lenses,[10] biosensors,[11] and plasmonics.[12] In the X-ray field, they are at the core of phase-based approaches. Phase-based approaches have the potential to revolutionize X-ray imaging, because they result in the generation of strong image contrast from features that present negligible attenuation differences against the background they are immersed in, such as soft biological tissues.[13] Here, nanostructuring opens new avenues to further advance phase-based X-ray imaging utilizing gratings, since the exploitation of coherent phenomena such as Talbot self-imaging requires the X-ray illumination to have a coherence length at least equal to, and ideally larger than, a grating period. Furthermore, the recent discovery of the infinite moiré effect opens new avenues to perform phase-based imaging with increased sensitivity and simplified setups.[14,15]

A key parameter to consider in order to perform this type of imaging is the need to attain a sufficiently large phase shift (typically π or $\pi/2$) at the desired X-ray energy, with higher energies ("harder" X-rays) providing access to a wider range of applications, but at the same time requiring taller structures to obtain a certain phase shift. Combined with periods of the order of hundreds of nanometers, this leads to high aspect ratios (>10, often much larger), that can be reduced only by employing higher Z materials such as gold (Au).[16] Concurrently, characteristics such as vertical profile for the trenches, regularity of the duty cycle and uniformity across the sample need to be taken into account. For this first proof-of-concept test, we are targeting energies of the order of 12 keV widely used in, for example, synchrotron research; in the future, we will strive to develop thicker structures in order to access a wider range of application, for example, medical imaging, which starts at ≈17.5 keV for mammography and requires energies of up to 100 keV in other, more challenging areas.

To accommodate these constraints, various techniques have been employed that predominantly rely on creating a polymer or silicon template with a conductive seed layer at the bottom of the trenches or conformally deposited along them for the

M. Michalska, A. Rossi, I. Papakonstantinou
Photonic Innovations Lab
Department of Electronic & Electrical Engineering
University College London
Torrington Place, London WC1E 7JE, UK
E-mail: i.papakonstantinou@ucl.ac.uk
G. Kokot
Jožef Stefan Institute
Jamova cesta 39, Ljubljana SI-1000, Slovenia
C. M. Macdonald, S. Cipiccia, P. R.T. Munro, A. Olivo
Department of Medical Physics and Biomedical Engineering
University College London
Malet Place, Gower St, London WC1E 6BT, UK
E-mail: a.olivo@ucl.ac.uk

subsequent electroplating of Au. The location of the seed layer dictates the metal deposition mechanism, which follows a bottom-up growth or from the sidewalls, respectively.

Although electroplating on polymer templates has the benefit of inducing a desirable void-free bottom-up metal growth due to an insulating character of polymer walls, the attainable aspect ratio is limited. Hence, the focus has turned to fabricating silicon templates via either deep reactive ion etching (DRIE) or metal assisted chemical etching (MACE). Since vertical side walls are a prerequisite, cryogenic DRIE is typically needed to avoid scalloping and etch taper under standard dry etching conditions, which in turn requires specialized equipment unlike MACE. The latter, first reported by Li and Bohn,[17] is less limited in terms of aspect ratio due to the highly localized electrochemical reaction occurring on silicon-metal catalyst interface in addition to being facile, cost-efficient, and scalable.[7] Broadly, it relies on patterning of a noble metal (Au, silver, and platinum (Pt)) on silicon which acts as both etch mask and catalyst to reduce hydrogen peroxide (H_2O_2) in a an etchant solution (hydrofluoric acid (HF) and water). During the oxygen reduction, electron holes are generated and injected into the underlaying silicon oxidizing it to silicon dioxide (SiO_2), which is subsequently etched by HF making the metal catalyst sink down. To date, the technique has been largely explored, particularly, in terms of etch rates, porosity, and etch profile, which can be tuned by substrate choice (resistivity, doping type), catalyst (type, porosity), H_2O_2/HF ratio, alcohol additives, temperature, supporting structures etc.[8,16,18] However, there are still two main challenges when the reactions need to be carried out at the nanoscale pitch and high aspect ratio. These include 1) stiction and agglomeration of structures during drying step and 2) taking advantage of a bottom-up metal electroplating from the existing seed layer.

The first issue occurs with an increasing grating height, and it is dependent on the mechanical properties of the used material and the forces acting upon it.[19] There is a maximal lamella height before an irreversible collapse occurs, mainly attributed in the literature to van der Waals forces, as well as capillary forces between the silicon surface and liquid–air interface during the drying process.[20] A prevention of collapse behavior is fundamental in preserving pattern-induced properties (optical etc.) as well as allowing for a conformal coating or gold filling. Until now, the issue has been solved by either employing sophisticated post-etching drying steps (critical point drying (CPD),[21] freeze drying[22]) or adding transversal supporting structures such as bridges.[23] The former requires special equipment and has limited scalability (CPD in particular). The latter complicates the design so that more complex methods are required to create a pattern in the first place, such as E-beam lithography, as opposed to simple laser interference lithography (LIL). Alternatively, MACE in the gas phase has been demonstrated to work,[7] albeit again requiring a bespoke setup instead of an ordinary wet bench, which is one of the aspects making this etching approach so attractive.

It appears appealing to utilize the remaining post-MACE catalyst – uniquely located at the bottom of the trenches – as a conductive seed layer for the subsequent bottom-up electroplating. However, in practice, this is not easy to achieve, and a mixed growth is often favored. This likely originates from the semiconducting character of silicon walls and the presence of some

level of porosity resulting from the etching process itself, which acts as nucleation sites.[24] To attain insulating walls, at least 150 nm of oxide layer is required to ensure large enough electrical resistivity,[25] which puts a limit on the pitch of the grating. For a larger pitch, on the other hand, this can be achieved via, for example, thermal oxidation. Yet, a change in a duty cycle needs to be factored in the design due to the nature of silicon oxidation itself. Some additives in the electrolyte may be incorporated to promote preferential plating at the bottom.[26,27] Alternatively, one can use chemical or physical vapor deposition (CVD or PVD, respectively) to conformally coat the walls with a seed layer and therefore induce the growth from the sidewalls toward the middle of the trenches. Within CVD approaches, atomic layer deposition (ALD) is unrivaled to accommodate any pattern resolution, and it has been shown by Miao at al.[28] to work for the nanogratings of 200 nm period, which were ultimately filled with Pt. Although PVD is thought to be less suitable for nanogratings, we show here that gratings with a half-pitch of ≈200 nm can be successfully sputtered to achieve electrical continuity. We find this to be strongly dependent on the quality of the adhesive layer. It is noteworthy that PVD is significantly cheaper and easier to implement within the process, and the entire step takes 1.5 h instead of several hours for a typical ALD step. Additionally, highly uniform sidewalls-growth can serve for halving the pitch in a similar manner as iterated spacer lithography.[29,30]

In this paper, we present a simple fabrication method, which consists of laser interference and nanoimprint lithography, MACE, and electroplating, for X-ray nanogratings with high aspect ratios (>40). This is enabled by our post-MACE drying step, which effectively minimizes the stiction of the nanostructures. In the electron microscopy community, evaporation of a low surface tension hexamethyldisilazane (HMDS) is a known drying alternative to CPD, used to preserve morphology of biological specimens.[31] Here, we successfully adapt it to silicon and show experimentally approximately twofold improvement in preventing the lamellae from collapsing when compared to drying from water, thus achieving ≈7 µm tall, defect-free nanogratings. We interpret that it is the HMDS chemical ability to lower surface energy of the gratings that also contributes to the effect. However, as we will discuss later, we observe a pronounced discrepancy between the theory predictions for maximal grating height and experimental observations. We identify that this divergence is in part caused by the incorrect assumption of the grating deflection axis and derive a condition for when the corner of the lamella will deflect first. Nevertheless, this approach allows to maintain the simplicity of the design and processing steps by being fast (minutes) and removing the need for special tools. While it can impact other fields where the collapse behavior constitutes a problem, here it allows us for a successful deposition of a conformal gold seed layer via sputtering and high-density gold filling of the trenches. Alongside detailed characterization via electron microscopy and other methods demonstrating that the design goals have been achieved, we also exposed one of the fabricated gratings to a hard (12.2 keV) monochromatic X-ray beam at a synchrotron facility and used the resulting diffracted powers to gain additional insight on the gratings' structure and their future usability as imaging devices.
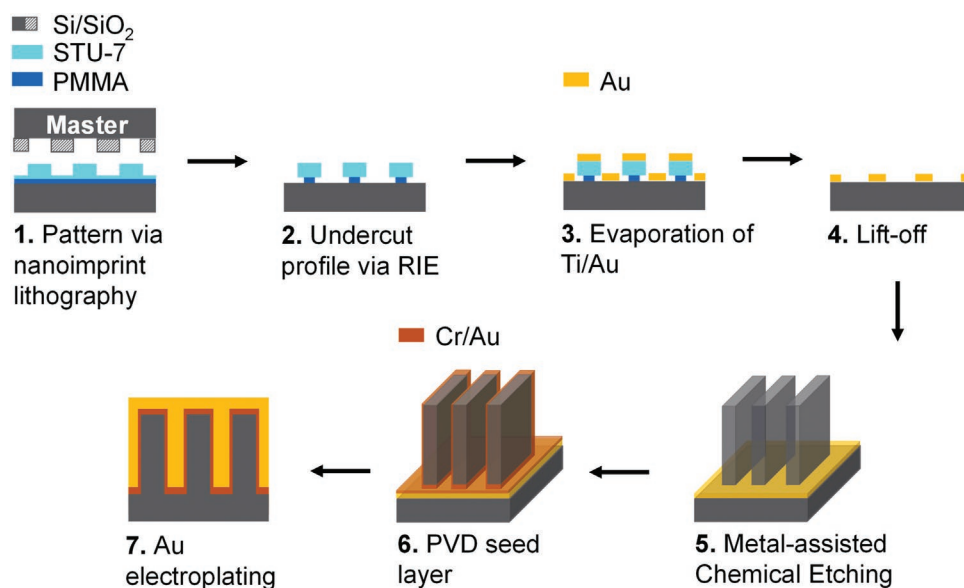
Figure 1. Overview of the nanogratings' fabrication. 1) The process begins with pattern generation via nanoimprint lithography (NIL) by stamping a master (prepared by laser interference lithography (LIL)) onto a polymer bilayer. 2) The bilayer facilitates an undercut profile, which is formed by reactive ion etching (RIE), followed by 3) e-beam evaporation of a metal catalyst. 4,5) After the lift-off process, which defines an etch mask, metal assisted chemical etching is performed yielding high-aspect ratio nanogratings. 6,7) Finally, a conformal conductive seed layer is sputtered onto the grating allowing to subsequently fill the trenches with gold via electroplating.

2. Results and Discussion

Figure 1 demonstrates fabrication steps, which, broadly speaking, include a generation of linear grating pattern (1–4), its transfer into silicon by MACE (5), and gold electroplating from a sputtered seed layer (67).

Specifically, the process begins with a master preparation followed by its replication via nanoimprint lithography (NIL; Figure 1, step 1). To prepare the master, we pattern a photoresist on a silicon wafer with a SiO$_2$ layer of 300 nm by means of LIL using a one-mirror Lloyd's interferometer setup (Figure S1, Supporting Information). Subsequently, we transfer the pattern into glass by reactive ion etching (RIE) and CHF$_3$/Ar plasma with varying H$_2$ content. The latter allows for a convenient tuning of the grating width and, in turn, of the duty cycle as we recently reported[32] – the higher the H$_2$ flux, the larger the duty cycle (Figure S1, Supporting Information).
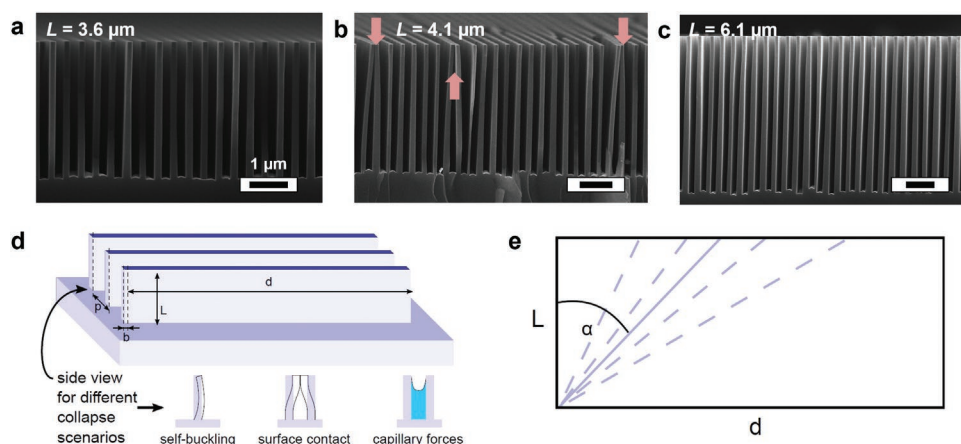
We then use NIL to replicate the master and prepare a series of patterns for the subsequent etching (Figure 1, step 2). Such pattern generation is cost-effective, fast and scalable; when done on a bilayer, it also allows lift-off.[33] Here, we stamp the master

on the bilayer consisting of poly(methyl methacrylate) (PMMA) sacrificial layer and STU-7 NIL resist (**Figure 2**a). The thickness of both layers needs to be optimized so that both residual layers are minimal to prevent a prolonged oxygen breakthrough, which would otherwise lead to a significant change in duty cycle (Figure S2, Supporting Information). Note that the thickness of STU-7 can be precisely calculated by knowing the pattern volume of the master. We achieve undercut by dry etching in oxygen plasma and taking advantage of the difference in etching rates between the layers and optimizing the etching time (Figure 1, step 2 and Figure 2b,c). The inset in Figure 2c presents the resulting gold pattern (2 nm titanium (Ti) and 15 nm Au) after electron beam (e-beam) evaporation (Figure 1, step 3) and lift-off (Figure 1, step 4).

In the next step (Figure 1, step 5), we perform MACE at standard conditions as previously described (see Experimental Section),[8] while carefully controlling the temperature. We find the temperature to be the most sensitive parameter to permit vertical etch, and thus features of high aspect ratio. Hence, the etching is conducted in an ice bath (≈7 °C). This slows down the transport and, crucially, it prevents catalyst mobility at the
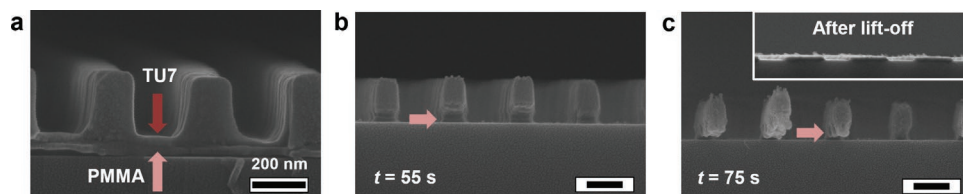
Figure 2. Bilayer lift-off process via nanoimprint lithography. Scanning electron microscopy (SEM) images of PMMA (bottom layer) and STU-7 (TU7; upper layer) layers nanoimprinted before a) and after descumming of the sacrafical layer for 55 and 75 s (b and c, respectively). An inset in (c) shows 15 nm of Au catalyst on 2 nm of Ti adehsive layer on silicon, which were electron beam-evaporated and lifted-off, in order to define the etch mask for the subsequent MACE step.

**ADVANCED
SCIENCE NEWS**
www.advancedsciencenews.com

**ADVANCED
FUNCTIONAL
MATERIALS**
www.afm-journal.de

Figure 3. The solvent effect after the post-MACE drying step on the gratings' integrity. SEM images of nanogratings after MACE, dried directly from water a,b) and using our HMDS approach c). Scale bars are 1 μm. d) A schematic of the grating and its dimensions used for modelling. The deflection is assumed along d axis. e) A shematic demonstrating the corner bend with several possible deflection axes (purple, dashed). The axis leading to minimal elastic restoring force is drawn as a solid purple line and the α angle from Equation 1 is indicated.

expense, however, of the etching rate ($\approx$45 nm min^{-1}). Note that catalyst movements such as rotation and folding can lead to interesting patterns,[34] albeit limiting the attainable aspect ratio because of the additional strain introduced by such movements. **Figure 3**a presents a defect-free nanograting of height $L = 3.6$ μm. With an increase in the etching time, however, we reach a height limit, above which the stiction between lamellae occurs during the drying step, deteriorating the pattern (Figure 3b).

Having assumed that capillary action is a driving force of the collapse behavior, we hypothesize that drying by evaporation of a low surface tension fluid like HMDS could minimize the effect. After all, HMDS is successfully used in the preparation of biological samples for electron microscopy. Such process relies on fixing the specimen in glutaraldehyde, its gradual dehydration in increasing ethanol (EtOH) concentrations, and immersion in HMDS, followed by air-drying. Remarkably, transferring the nanograting directly from water into 50% and then 100% EtOH, followed by dipping in HMDS, and allowing it to air-dry, preserves the vertical profile and pattern integrity as shown in Figure 3c. Etching for 2.5 h leads to gratings of $\approx$7 μm height with well-preserved patterns that we will use for further investigations.

To elucidate the underlying mechanism, we vary the drying conditions (**Table 1**, samples 1–4) to find out that both ethanol and HMDS are required as an intermediate and final solvent, respectively, to achieve the desired effect. We assess the effect based on SEM imaging of the cross sections and top views across the entire surface as well as by a visual inspection. As expected, unlike biological specimens necessitating penetration

through a mesh of their internal and fragile structures, here one ethanol concentration is sufficient to replace water, due to the solid nature of silicon. A direct transfer of the sample from water to HMDS (sample 4) leads to an observable phase separation on the drying surface, due to the high immiscibility of the liquids. While the HMDS phase dries instantly, the water phase requires several hours and leaves a distorted pattern behind, assessed by SEM top view micrographs (Figure S3, Supporting Information). The pattern distortion changes the optical properties of the sample, and the collapsed areas can be noted upon a visual inspection and clearly distinguished from the defect-free diffractive regions (Figure S3, Supporting Information, light and dark regions). Interestingly, despite EtOH and HMDS having similar surface tensions (22.4 and 18.2 mN m^{-1}, respectively), drying only from EtOH (sample 3) leads to the structural collapse (Figure S4, Supporting Information). These experimental results suggest that capillary forces are indeed an important piece of the puzzle, although as we demonstrate not in a sense typically considered in existing calculation approaches.

HMDS is routinely employed in cleanroom processes as an adhesion promoter prior to the photoresist coating. On a water-free surface, it works by its ability to chemically bond its silicon atom to the oxygen of oxidized surface. After the HF etching, which removes SiO_2, we expect the predominant coverage of the surface with hydride group with, however, a small percentage of hydroxylation due to the presence of water and hydrogen peroxide.[35] We compare water contact angles, θ, on the non-patterned silicon surface before and after MACE (sample nitrogen-dried directly from water) and we note a significant increase in θ (Figure S5, Supporting Information), which confirms the domination of hydride groups. After drying the sample with HMDS, θ increases further (from 48° to 87°), indicating chemically bonded molecules, and hence, the presence of some hydroxylation induced during the etching. We also measure the water contact angle on grating 2 (Table 1) and obtain $\theta = 147°$.

The hydrophobic character of the gratings after the HMDS treatment is sufficiently robust to prevent inducing the collapse

Table 1. Summary of the drying protocols.

Sample ID	H$_2$O	EtOH 50%	EtOH 100%	HMDS	Effect
1	x	x	x	X	defect-free
2	x	–	x	x	defect-free
3	x	–	x	–	collapse
4	x	–	–	x	collapse

**ADVANCED
SCIENCE NEWS**

www.advancedsciencenews.com

**ADVANCED
FUNCTIONAL
MATERIALS**

www.afm-journal.de

behavior after sonicating samples in water (15 min; the sample floats on the water-air interface). Repeating the same test with EtOH results in collapsed edges of the grating, albeit a careful inspection across the sample reveals a well-preserved pattern (Figure S6, Supporting Information). Upon removing the silane in oxygen plasma, which also does not damage the pattern, collapse can be induced by placing the sample in water. This further validates that a change in surface energy plays a role in protecting the pattern.

We now compare our experimental results with theoretical models that predict collapse behavior to better understand the underlying mechanism as well as the limits of our approach and how to potentially overcome them. Such limit can be expressed as the maximal lamella height, L_{max}, before an irreversible collapse occurs. The particular force responsible for the collapse remains elusive as we confirm that the standard calculations greatly overvalue L_{max}, though we make important steps toward understanding how exactly the lamella collapses based only on restoring elastic force arguments.

We consider a cuboid lamella of width b = 80–250 nm (matching our experiment), and length, d = 1 cm (Figure 3d). We begin our analysis (see Supporting Information for details) with the traditional assumption that deflection of a cuboid happens along d and in the direction of the smallest dimension, which in our case is b. We then follow several scenarios for forces that could lead to buckling.

We start with self-buckling (SB) – a collapse initiated solely by gravity acting on the lamella – and find that the prediction from the Greenhill result of L_{maxSB} = 5.3 mm vastly overestimates the experimental value L_{max} < 10 µm, even before we introduced the HMDS method. This large discrepancy has been consistently found in experiments with distinct protrusion geometries.[36,37] Figure S7 (Supporting Information) shows the achieved, albeit not ultimate, experimental limits of the aspect ratio of nanogratings after introducing HMDS-mediated drying. While there is no doubt that 7.2 µm tall gratings (aspect ratio 43) can be achieved, the images of 12.2 µm tall patterns (aspect ratio 117) imply that the collapse here is more likely driven by our inability to control the etching anisotropy (Figure S7b, Supporting Information). Multiple regions exhibit defect-free characteristics as demonstrated in Figure S7c,d (Supporting Information). Although this obstacle prevents us from showing a true limit for our drying approach (hence, L_{max} with inequality sign), it does not prevent us from further discussing the theory of the underlying mechanism.

With self-buckling ruled out, we now consider scenarios where a force bends two lamellae until they come into contact. A good candidate is capillary forces, because we experimentally know the collapse happens during the drying process. We compare the capillary force for our geometry, where we make the usual simplification of two infinite parallel lamellae, to the elastic restoring force and calculate L_{max} for capillary force, L_{maxCF} = 107 µm. This result reveals that the capillary force, as obtained with the underlying assumptions for two infinite parallel lamellae, is not large enough to bring them in contact at the measured L_{max}.

Surface interaction is another candidate to explain the lamella collapse. Following the result from Hui at al.[37] and using our notation for geometrical parameters, we obtain an L_{max} for

surface energy interaction, L_{maxSE} = 2 µm, which is indeed less than the experimentally determined L_{max}. The computed L_{maxSE} can be larger, if one is to include electrostatic interaction, as has been shown for pillars.[19] HMDS treatment of silicon changes the contact angle (Figure S5, Supporting Information), which demonstrates that van der Waals forces between treated and non-treated surfaces are different. Those forces are responsible for sticking of surfaces together.[38,39] Consequently, the surface energy that enters Equation S3 (Supporting Information) is modified – L_{maxSE} increases by a factor of three when surface energy is lowered by two orders of magnitude. Yet, we cannot brush off the fact that the surface interaction scenario comes with the surfaces already in contact. However, the result does assure us that any lamella height above L_{maxSE} will result in a collapse, if we apply a force great enough to bend them toward each other.

Another suggestion for a lateral force on the lamella is the Laplace pressure variation due to surface roughness and lamella thickness variation. As has been pointed out before, the Laplace pressure differences do not exist if the liquid between each lamella space is not strictly separated (as would be the case for infinitely long lamellae). For lamellae with finite length, during the drying, the liquid stays connected at the bottom edges outside of the grating. Nevertheless, variations in b and defects present in experiments can influence the local bending condition.

Despite having already established that capillary forces between two infinite parallel lamellae are not responsible for the collapse, we have experimental evidence suggesting capillary action is not to be discarded. Figure S6 (Supporting Information) shows a grating with L close to L_{max}, where the lamella deformed at the corners and is still standing unbent in the central part. The deformation does not happen around the axis assumed for the infinite parallel lamellae (Figure 3d) but rather a differently oriented, much shorter axis. We calculate the elastic restoring force for the lamella corner, compare it to the same type of force for the lamella cuboid, and derive a condition for lamella length (d) at which the bending of the corner is preferable (i.e., the force needed to bend it is the smallest, (Figure 3e)):

$$d > \frac{4\,L^3}{3\sin(2\alpha)\delta^2} \tag{1}$$

Where α is the angle between the vertical lamella edge and the axis of corner buckling (see Figure 3e) and δ is the deflection, which in our case is half the pitch ($\delta = p/2$). The right side of Equation 1 is minimized at $\alpha = \pi/4$, which predicts the optimal buckling angle for the corner. In the range of our experimental values for L, δ, and d, Equation.1 is always fulfilled, thus predicting that corner collapse happens first. The corner of the lamella is a strong pinning point for the liquid interface, and we experimentally influence L_{max} by changing the drying agent. Unfortunately, an analytical expression for a capillary force in a situation described here is lacking in the literature and is beyond the scope of this paper. However, a scenario, where the lamellae touch their surface first at the corners of the grating and then continue the collapse by mechanism of surface energy is supported by our analysis.
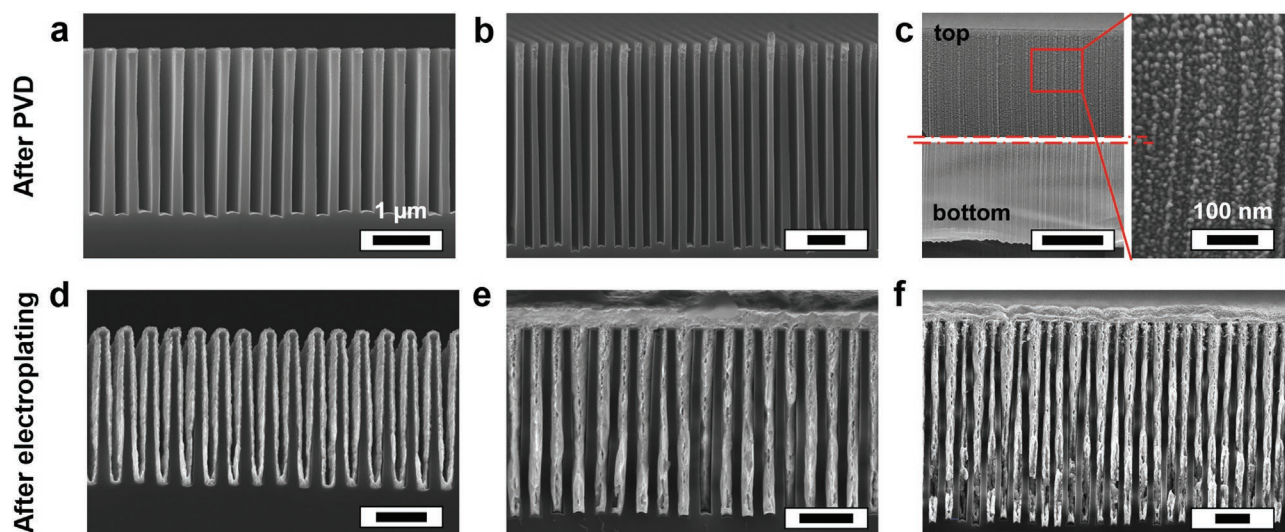
Figure 4. A seed layer on silicon mold and gold-filled trenches by electroplating. a–c) SEM cross sectional images showing the Cr/Au seed layer on high-aspect ratio nanogratings and d–f) the results of gold electroplating. The seed layer was succesfully sputtered on gratings with two heights: a) $L = 3.2$ μm and b) $L = 6.1$ μm. c) A magnification of a face-view of the lamella confirms the seed layer deposition and reveals its granular structure ($L = 6.1$ μm). d) A conformally electroplated gold following the silicon mold can be utilized for halving the period. e,f) Trenches of high-aspectratio silicon mold fully filled with gold. Aspect ratios are 16 (e) and 30 (f). Scale bars are 1 μm, unless stated otherwise.

After successful fabrication of the vertical grating, we now fill the space between the trenches with gold in order to prepare it for the subsequent evaluation of the X-ray performance. Silicon is the material of choice for gratings fabrication due to its very good robustness, its relative X-ray transparency, and low cost. A conductive layer (e.g., Au, Pt, copper) reduces the overpotential necessary to allow plating, driving the nucleation and growth of metal onto itself. The quality and nature of the seed layer, combined with the plating method, can change the electrochemical deposition in terms of plating rate, morphology, and density.[40,41] To ensure good electrical contact and prevent any mechanical damage during handling the nanoscale gratings, we introduce a frame surrounding the design (Figure S9, Supporting Information). This proves to be of paramount importance at such scales for certain geometries (see Text 2, Figure S10, Supporting Information).
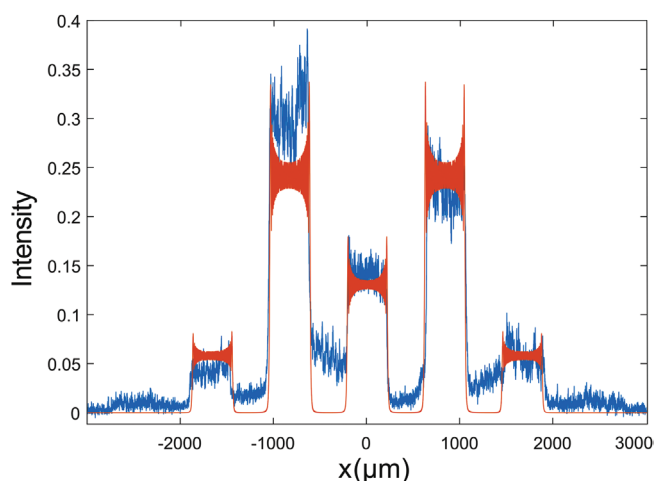
We first attempt an electroplating on the remaining post-MACE gold catalyst layer, which is conveniently located at the bottom of trenches. Unfortunately, this approach led to a mixed growth, likely due to some porosity of the sidewalls. We therefore follow a different approach to force an electrochemical deposition in a conformal way by depositing a seed layer of the same material (Au) via sputtering (Figure 1, step 6). We demonstrate that high-pressure sputtering can successfully deposit a quality seed layer on high-aspect ratio nanogratings (**Figure 4**a–c). Here, we find that an optimal thickness of adhesive layer (chromium (Cr) in this instance) is key to achieve an electrical continuity across the grating. An excessively thin layer leads to a patchiness in the electroplated gold, which follows the areas where a continuous seed layer was present (Figure S8a–c, Supporting Information). Doubling the time of Cr deposition while maintaining the Au sputtering conditions (7.5 min) results in a full coverage along the sidewalls with a mosaic structure (Figure 4c; Figure S8d, Supporting Information), similar to the one obtained by ALD.[14] We expect further

optimization to be required for higher aspect ratios (remains to be investigated). Finally, we successfully electroplate the gratings across a full length of the trench (Figure 1, step 7; Figure 4d–f, Figure S8ef, Supporting Information) by using a sulphite-based gold plating solution and a direct cathodic current (see Experimental Section).

The design of the gratings is optimized to diffract hard X-rays with low absorbance, by producing a phase shift of π[15] at the design energy of 12.2 keV, readily available at the Diamond Synchrotron Light Source (United Kingdom). One of them was tested at the I13-1 beamline of above synchrotron facility for its diffractive ability. We tested a grating with a 414 nm period, a ≈50% duty cycle, height of 3.2 ± 0.2 μm, and an estimated Au density of 87%. The sample was placed at 3.3 m from a detector (see Experimental Section) and exposed to a monochromatic beam with energy of 12.2 keV, with a pre-collimating beam aperture width of 440 μm in the direction orthogonal to the grating trenches. The diffraction orders' intensities are a quantitative measurement of the grating performance, and they depend on the phase modulation induced by the silicon and Au lamellae.

Variations in attenuation/phase shift due to the slight deviation of the X-ray beam direction as a consequence of it being redirected into the ±1 diffraction orders can be neglected, as the diffraction angle is of ≈250 microradians which imply a lateral penetration of <1 nm into a 3.2-micron thick structure.

In practical terms, when one considers the lateral size of each X-ray "beamlet" traveling through the non-absorbing parts of the grating, this means that <0.5% of the beamlet width that would travel through the aperture will travel through the gold. Not only is this a negligible fraction: for both the +1 and the −1 orders, this is accompanied by a corresponding "<0.5% fraction" at the other side of the beamlet that would have travelled through gold but is sent into the aperture, creating counteracting effects that effectively cancel each other out. Conversely,

**ADVANCED
SCIENCE NEWS**

www.advancedsciencenews.com

**ADVANCED
FUNCTIONAL
MATERIALS**

www.afm-journal.de

Figure 5. The intensity profile of the diffracted X-ray beam. The blue line and the orange lines show the experimental data and the simulated signal, respectively, for a 12.2 keV beam diffracted by a 414 nm-period and 3.2 μm tall grating with a gold density of 87%.

the total thickness of the lamella and the silicon substrate is ≈200 μm, which can cause a non-negligible attenuation of the beam at the used energy. Although this can be reduced by using a higher energy, the transmitted intensity was sufficient to quantitatively estimate the diffracted powers. A higher energy, however, would also require even higher aspect ratio grating to produce the same phase shift values. This will be the subject of future research once the imaging performances of the nanogratings have been fully tested and validated.

The simulated intensity profile (**Figure 5**, orange line) largely agrees with the experiment (blue line), providing further confirmation that the design specifications were met. The grating successfully splits the beam into several visible diffraction orders, which we collected up to the 2nd order. The 1st orders collect the highest intensity, equal to ≈24% of the transmitted flux. The asymmetry between the 1st diffraction orders may be attributed to some tapering and catalyst mobility slightly varying lamellae shape.[28] Both can be corrected by fine-tuning oxidant/etchant ratio and more efficient temperature control by mixing (see Experimental Section), respectively.[42,43] Likewise the excess intensity between diffracted orders can be attributed to residual grating imperfections and especially to X-ray scattering, notably by air considering there was a 3.3 m grating-to-detector distance in the used setup, without an evacuated tube.

3. Conclusion

Attaining high-aspect ratio, dense nanostructures is a long-standing challenge being systematically addressed by advances in fabrication processes. Our method shows significant improvements in respect to the state-of-the-art in fabrication of nanogratings, which typically requires expensive and time-consuming steps such as DRIE for etching or ALD to introduce seed layer. In this paper, instead, the sputtering gives a satisfactory seed layer coating and can be performed within 120 min. Furthermore, to the best of our knowledge, we demonstrate

for the first time a successful etching of high-aspect ratio sub-micron gratings without additional supporting structures via wet MACE for X-ray applications. We achieve it with our new drying step based on HMDS that replaces more sophisticated processes. Finally, the fabricated gratings possess the expected diffractive abilities when exposed to a monochromatic X-ray beam, with most of the transmitted flux being redirected to higher order energies. This is a fundamental property for interferometric phase contrast imaging and the sub-micron period of the grating can extend its applicability to low coherence compact sources, and, ultimately, find applications across the life and physical sciences. Besides X-ray field, we envision the findings related to the fabrication of nanogratings and method to prevent their collapse to be far reaching, relevant to research in displays, optical communications, lasers, security features, and more.

4. Experimental Section

The fabrication process consists of 1) master preparation via laser interference lithography and glass etching, 2) master replication via nanoimprint lithography, 3) metal assisted chemical etching, and 4) electrodeposition of gold (Figure 1).

Master Preparation: Master with a linear grating of period $p = 400$ nm was prepared via LIL using a Lloyd's mirror interferometer setup as it was previously reported.[30] First, a silicon wafer (p-type, boron-doped, <100>, 1–10 Ohm cm, 675 μm thick; MicroChemicals) with 300 nm of SiO_2 layer was cleaned with acetone and isopropyl alcohol. A photoresist ma-N 400 (Microresist Technology) was diluted 2:1 with 4-methyl 2-pentanone, spin coated onto the wafer at 4000 rpm, and baked at 100 °C for 2 min. Subsequently, the wafer was illuminated at 24° for 90 s using the free-space UV laser with a beam diameter of ≈1 mm (IK3201R-F by Kimmon; Class 3B; 25 mW; 325 nm; CW; single mode TEM00). The pattern was then developed using AZ 726 MIF (5:1 dilution with deionized water; Microchemicals) for 2 min. An oxygen descum etch was performed to remove any residual photoresist. The pattern was registered in glass by reactive ion etching (PlasmaPro NGP80 RIE, Oxford instruments) under the following conditions: CHF_3 15 sccm (standard cubic centimeters per minute), Ar 50 sccm, 215 W, 3 mTorr, and 20 °C. To increase the grating width, H_2 was used at 6 sccm.

Nanoimprint Lithography: To replicate the pattern for a subsequent lift-off process, which requires an undercut profile, NIL was performed on a bilayer deposited on silicon. First, a silicon wafer (p-type, boron-doped, <100>, 1–10 Ohm cm, double polished, 200 μm thick; MicroChemicals) was cleaned as above, and subsequently spin coated with 1) PMMA 950 A2 (MicroChem Corp.) at 2000 rpm and baked at 160 °C for 5 min, followed by 2) STU-7 (Obducat) and baked at 100 °C for 1 min. Depending on the master profile, STU-7 was diluted accordingly to achieve a minimal residual layer after the imprint. The NIL process was performed on EITRE 3 (Obducat). The master was first replicated into an intermediate polymer stamp (IPS; Obducat) at 155 °C and 30 bar for 20 s. Transfer of the negative pattern into the STU-7 was operated at 70 °C and 40 bar for 60 s with 120 s of UV curing. The undercut profile was achieved by O_2 RIE (20 sccm, 50 W, 50 mTorr) where PMMA layer was intentionally over-etched (75 s).

Metal Assisted Chemical Etching: First, the metal catalyst (2 nm Ti and 15 Au) was electron beam evaporated onto the pattern with deposition rate of 0.1 nm min⁻¹. Lift-off was performed in dimethyl sulfoxide via sonication at 65 °C for 5 min twice. Prior to the MACE, samples were subjected to O_2 plasma for 1 min, which increased the etching rate threefold. The MACE was carried out in a solution comprised of 5.3 M HF, 0.25 M H_2O_2, and 50 M H_2O at ≈7 °C for 1–5 h, and then rinsed thoroughly with H_2O and stored in H_2O until the drying step. To achieve and maintain the low temperature, a beaker containing the

samples was placed in an ice bath. The ice was replenished every 20 min and a manual mixing was employed every 5 min. Due to technical constraints when handling HF, other mixing methods were unable to be implemented, which are planned to address for the future processes. The samples were handled carefully to avoid air-drying, which would otherwise lead to agglomeration of the Si lamellae. The drying was performed by transferring the samples from water to absolute ethanol, and subsequently to hexamethyldisilazane (HMDS, 100%) for 2 min. Finally, the samples were allowed to air-dry under the chemical hood for 10 min.

Electrodeposition: To realize the Au electrodeposition, a conductive seed layer was deposited by means of PVD (Lesker PVD75 Sputter Coater system). First, a Cr adhesive layer was applied (DC 500 W, 5 mTorr) with deposition rate of 11 nm min⁻¹. Next, Au was deposited (DC 50 W, 3.75 mTorr) with the rate of 6.5 nm min⁻¹. As prepared samples were electroplated in NB Semiplate Au 100 (Arsenic-based, MicroChemicals) by using the current density of 0.112 Ma cm⁻² at 30 °C. The current was applied using a PGSTAT204 (MetrOhm) supported by the software NOVA.

Material Characterization: Cross-section and top view SEM images were taken by Carl Zeiss XB1540 SEM and SmartSEM software (equipped with tilt correction) at 2–10 kV operating voltage. Prior to the imaging, samples were manually cut into smaller sections and some samples were sputter-coated with Au. Note, the manual cut can induce defects, whose origin, however, was apparent when analyzing the micrographs. ImageJ was used for statistical analysis of the nanostructure dimensions such as height and widths (with 50 quantities measured).

The pitch and duty cycle of the gratings were measured using top view images at SEM (e.g., Figure S1c, Supporting Information) by the developed Python script. The script acquired and binarized the image finding the edges of the gratings using Canny edge detection. The average period and width of the grating were then measured from the middle points between the detected edges. The image magnification was chosen as high as possible to have a consistently low pixel/nm ratio to reduce the inaccuracy of the algorithm.

Electrochemical Deposition Characterization: The gold deposit was observed by the SEM and showed a compact structure growing from the sidewalls inward (Figure 4). After filling up the trenches, a gold overgrowth atop occurs. To control the latter, the mass m of gold to be deposited to completely fill the trenches was predicted using Faraday's law:

$$m = \frac{I\, t\, M_w}{z\, F} \tag{2}$$

Where I is the direct current applied, t is the total plating time, M_w is gold molecular weight, z is valence number, and F the Faraday's constant. For each sample, the surface area A to immerse in solution was measured before the plating using ImageJ and its mass using a precision balance. Therefore:

$$\rho V = \frac{I\, t\, M_w}{z\, F} \tag{3}$$

$$\frac{\rho A h}{2} = \frac{I\, t\, M_w}{z\, F} \tag{4}$$

$$\frac{\rho h}{2} = \frac{I/A\, t\, M_w}{z\, F} = \frac{J\, t\, M_w}{z\, F} \tag{5}$$

Where ρ is the bulk gold density (19.3 g cm⁻¹), V is the volume to electroplate, h is the height of the gratings, and the factor ½ accounts for the volume of the trenches to be plated (assuming a duty cycle of 50%). J is the current density applied during the plating and it was kept constant to have the same deposition rate for every sample. Using this equation, plating time and deposited mass were estimated. The values of final mass, time, and volume plated agreed with the predicted values. The method is further validated by the fact that the trench over-plating consistently started after the time predicted for the trenches

to be filled. The onset correlates with a negative shift of 0.01–0.02 V, clearly visible in the in-operando voltage profile of the software NOVA (see Figure S8g, Supporting Information). The different environment where the gold grows, from a narrow trench to the top of the structure, changes the ions concentration at the metal-electrolyte interface, thus negatively changing the voltage needed to maintain the set current density. Consequently, the negative shift can act as a probe to calibrate the metallization to occur only in between high-aspect ratio structures without overfilling.

X-Ray Performance: The diffractive performance of one of the gratings was tested at the I13-a beamline of the Diamond Light Source (Didcot, Oxfordshire, UK) using a hard X-ray monochromatic beam of photon energy 12.2 keV. This energy was selected as it was expected to result in a π phase modulation according to the design specifications of the grating (414 nm-period and a 3.2 ± 0.2 µm height, trenches filled with gold at 87% of its nominal density).

The collimated beam size was defined by using a set of X-ray slits upstream the grating to be 440 µm to prevent the diffracted orders of the grating from overlapping at the detector. The detector (a PCO edge scientific CMOS coupled to a scintillator via an objective, resulting in an effective pixel size of 0.8 µm) was placed at 3.3 m from the grating. This arrangement allowed resolution of the 0th and the ±1st diffraction orders which were separated by 840 µm at the detector. To image the higher orders, the detector was moved laterally in both directions. To merge the images, an intensity profile of each image was taken, with the overlapping features identified and averaged prior to the merging. Images of the unperturbed beam, that is, without the grating (I_0) and with the beam off (I_{dark}) were collected to apply flat and dark-field corrections to the grating image I as per Equation (6):

$$\tilde{I} = \frac{(I - I_{dark})}{(I_0 - I_{dark})} \tag{6}$$

Where $\tilde{I}$ is the corrected image (a profile from which is plotted in Figure 5) used to calculate the diffraction order powers.

Design of Gratings and Validation Simulations: The fabrication method allows for gratings to be designed to achieve a specified phase modulation between the Au filled trench, and the silicon lamellae at a given X-ray energy. For example, if a phase modulation of ϕ was desired at an energy of E, then the necessary trench height, L, can be determined by:

$$L = \frac{\phi \lambda_E}{2\pi \left(\delta_{Au}(\rho_{Au}, E) - \delta_{Si}(\rho_{Si}, E) \right)} \tag{7}$$

where λ_E is the wavelength at energy E, and δ_{Au}, δ_{Si}, are the material deltas which themselves are a function of the material densities, ρ_{Au}, ρ_{Si}, and the energy E.

In house beam propagation software[44] was used to perform wave optical simulations of the proposed gratings and of the experimental setup. The simulations explicitly include the grating structure, effective source to grating distances, as well as grating to detector distances. The grating used in the experiment at the I13 beamline of the Diamond Light Source (Didcot, Oxfordshire, UK), was designed to attain a $\phi = \pi$ phase modulation at an energy of 12.2 keV. Assuming a 100% density of Au in the trenches, this requires a grating height of $L = 3.2$ µm. After comparison of the experimental results to simulations, it was determined that the density of Au in the trenches is likely 87% of nominal (bulk) Au density, and thus the achieved phase modulation of the 3.2 µm grating is less than π. This revised estimate of the achieved Au density can be used in the equation above to improve the accuracy of the target phase modulation.

Supporting Information

Supporting Information is available from the Wiley Online Library or from the author.

Conflict of Interest

The authors declare no conflict of interest.

Data Availability Statement

The data that support the findings of this study are available from the corresponding author upon reasonable request.

[1] M. S. Schmidt, J. Hübner, A. Boisen, *Adv. Mater.* **2012**, *24*, OP11.
[2] A. P. Yuda, P. Y. E. Koraag, F. Iskandar, H. S. Wasisto, A. Sumboja, *J. Mater. Chem. A* **2021**, *9*, 18906.
[3] J. He, Z. Yang, P. Liu, S. Wu, P. Gao, M. Wang, S. Zhou, X. Li, H. Cao, J. Ye, *Adv. Energy Mater.* **2016**, *6*, 1501793.
[4] P. Lecointre, S. Laney, M. Michalska, T. Li, A. Tanguy, I. Papakonstantinou, D. Quéré, *Nat. Commun.* **2021**, *12*, 3458.
[5] M. Michalska, S. K. Laney, T. Li, M. K. Tiwari, I. P. Parkin, I. Papakonstantinou, *Nanoscale* **2022**, *14*, 1847.
[6] M. Michalska, F. Gambacorta, R. Divan, I. S. Aranson, A. Sokolov, P. Noirot, P. D. Laible, *Nanoscale* **2018**, *10*, 6639.
[7] L. Romano, M. Kagias, J. Vila-Comamala, K. Jefimovs, L.-T. Tseng, V. A. Guzenko, M. Stampanoni, *Nanoscale Horiz.* **2020**, *5*, 869.
[8] C. Chang, A. Sakdinawat, *Nat. Commun.* **2014**, *5*, 4243.
[9] J. Y. E. Chan, Q. Ruan, H. Wang, H. Wang, H. Liu, Z. Yan, C.-W. Qiu, J. K. W. Yang, *Nano Lett.* **2022**, *22*, 8189.
[10] G. Quaranta, G. Basset, O. J. F. Martin, B. Gallinet, *ACS Photon.* **2017**, *4*, 1060.
[11] K. Cottier, M. Wiki, G. Voirin, H. Gao, R. E. Kunz, *Sens. Actuat. B Chem.* **2003**, *91*, 241.
[12] Z. Dong, M. Asbahi, J. Lin, D. Zhu, Y. M. Wang, K. Hippalgaonkar, H.-S. Chu, W. P. Goh, F. Wang, Z. Huang, J. K. W. Yang, *Nano Lett.* **2015**, *15*, 5976.
[13] A. Momose, T. Takeda, Y. Itai, K. Hirano, *Nat. Med.* **1996**, *2*, 473.
[14] S. K. Lynch, C. Liu, N. Y. Morgan, X. Xiao, A. A. Gomella, D. Mazilu, E. E. Bennett, L. Assoufid, F. de Carlo, H. Wen, *J. Micromech. Microeng.* **2012**, *22*, 105007.
[15] H. Miao, A. Panna, A. A. Gomella, E. E. Bennett, S. Znati, L. Chen, H. Wen, *Nat. Phys.* **2016**, *12*, 830.
[16] L. Romano, M. Stampanoni, *Micromachines* **2020**, *11*, 589.
[17] X. Li, P. W. Bohn, *Appl. Phys. Lett.* **2000**, *77*, 2572.
[18] C. Chiappini, in *Handbook of Porous Silicon*, (Ed.: L. Canham), Springer International Publishing, Cham **2014**, pp. 171–186.
[19] A. Mallavarapu, P. Ajay, S. v. Sreenivasan, *Nano Lett.* **2020**, *20*, 7896.
[20] A. S. Togonal, L. He, P. Roca I Cabarrocas, R. Rusli, *Langmuir* **2014**, *30*, 10290.
[21] A. E. Hollowell, C. L. Arrington, P. Finnegan, K. Musick, P. Resnick, S. Volk, A. L. Dagel, *Mater. Sci. Semicond. Process.* **2019**, *92*, 86.
[22] F. Koch, F. Marschall, J. Meiser, O. Márkus, A. Faisal, T. Schröter, P. Meyer, D. Kunka, A. Last, J. Mohr, *J. Micromech. Microeng.* **2015**, *25*, 075015.
[23] L. Romano, J. Vila-Comamala, K. Jefimovs, M. Stampanoni, *Adv. Eng. Mater.* **2020**, *22*, 2000258.
[24] C. N. Nanev, E. Saridakis, N. E. Chayen, *Sci. Rep.* **2017**, *7*, 35821.
[25] H. Zhou, F. G. Shi, B. Zhao, *Microelectron. J.* **2003**, *34*, 259.
[26] D. Wheeler, D. Josell, T. P. Moffat, *J. Electrochem. Soc.* **2003**, *150*, C302.
[27] D. Josell, T. P. Moffat, *J. Electrochem. Soc.* **2017**, *164*, D327.
[28] H. Miao, A. A. Gomella, N. Chedid, L. Chen, H. Wen, *Nano Lett.* **2014**, *14*, 3453.
[29] J. Vila-Comamala, S. Gorelick, E. Färm, C. M. Kewish, A. Diaz, R. Barrett, V. A. Guzenko, M. Ritala, C. David, *Opt. Express* **2011**, *19*, 175.
[30] S. K. Laney, T. Li, M. Michalska, F. Ramirez, M. Portnoi, J. Oh, M. K. Tiwari, I. G. Thayne, I. P. Parkin, I. Papakonstantinou, *ACS Nano* **2020**, *14*, 12091.
[31] F. Braet, R. de Zanger, E. Wisse, *J. Microsc.* **1997**, *186*, 84.
[32] M. Michalska, S. K. Laney, T. Li, M. Portnoi, N. Mordan, E. Allan, M. K. Tiwari, I. P. Parkin, I. Papakonstantinou, *Adv. Mater.* **2021**, *33*, 2102175.
[33] S. Si, M. Hoffmann, *Microelectron. Eng.* **2018**, *197*, 39.
[34] O. J. Hildreth, W. Lin, C. P. Wong, *ACS Nano* **2009**, *3*, 4033.
[35] D. Gräf, M. Grundner, R. Schulz, L. Mühlhoff, *J. Appl. Phys.* **1990**, *68*, 5155.
[36] S. Timoshenko, J. M. Gere, in *Theory of Elastic Stability*, 2nd ed., Dover Publications, Mineola, NY **2009**.
[37] C. Y. Hui, A. Jagota, Y. Y. Lin, E. J. Kramer, *Langmuir* **2002**, *18*, 1394.
[38] K. Autumn, Y. A. Liang, S. T. Hsieh, W. Zesch, W. P. Chan, T. W. Kenny, R. Fearing, R. J. Full, *Nature* **2000**, *405*, 681.
[39] W. Zhang, H. Wang, A. T. L. Tan, A. Sargur Ranganath, B. Zhang, H. Wang, J. Y. E. Chan, Q. Ruan, H. Liu, S. T. Ha, D. Wang, V. K. Ravikumar, H. Y. Low, J. K. W. Yang, *Nano Lett.* **2022**, *22*, 8917.
[40] S. Znati, N. Chedid, H. Miao, L. Chen, E. E. Bennett, H. Wen, *J. Surf. Eng. Mater. Adv. Technol.* **2015**, *05*, 207.
[41] A. Pei, G. Zheng, F. Shi, Y. Li, Y. Cui, *Nano Lett.* **2017**, *17*, 1132.
[42] Y. Zheng, C. Li, H. Hu, S. Huang, Z. Liu, H. Wang, *Jpn. J. Appl. Phys.* **2021**, *60*, 035003.
[43] P. Lianto, S. Yu, J. Wu, C. V. Thompson, W. K. Choi, *Nanoscale* **2012**, *4*, 7532.
[44] P. R. T. Munro, *J. Opt. Soc. Am. A* **2019**, *36*, 1197.